Radial impact test of aluminium wheels - numerical simulation and experimental validation

G. Previati, F. Ballo, M. Gobbi, G. Mastinu

Politecnico di Milano, Department of Mechanical Engineering,Via La Masa 1, Milan

Abstract

Safety is a crucial issue for automotive wheels, normally subject to severe dynamic working conditions. Severe indoor tests have been conceived and standardised to guarantee the required safety standards of vehicle wheels. This paper is devoted to the analysis and virtual simulation of the radial impact test of aluminium wheels, one of the most severe tests the wheel has to pass before production.

The radial impact test is simulated, for a number of different aluminium wheels, by means of a finite element model. The model includes tyre, wheel, striker and supporting structure. The actual structure of the tyre is modelled. Tyre damping is included through a Rayleigh model, whose parameters are experimentally identified. The wheel material inhomogeneity is taken into account by assigning different stress/strain curves to wheel rim and spokes.

A wheel instrumented with strain gauges has been used to validate the finite element model. An additional set of four families of different wheel types, equipped with different tyres, has been considered to asses the experimental variability and to compare the outputs of the corresponding impact models realized by the same procedure. The finite element model of the radial impact test has proven to be effective in reproducing the final plastic deformation of the wheel and thus to predict the compliance of the wheel design with the requirements coming from standards.

Keywords: Aluminium wheel, radial impact, tyre model, experimental test

1. Introduction

The two major concerns in the design of automotive wheels are safety and mass reduction (lightweight design) [1, 2, 3, 4]. Wheels are critical components for the safety of road vehicles and are subject to severe dynamic working conditions during the vehicle life. Lightweight design is the other important driver, not only to improve performance, but also for cost reduction.

Concerning safety, given their primary role, wheels are subject to severe and restrictive tests before production. Rotary bending [1, 3] and biaxial [5, 6, 7] fatigue tests are devoted to the assessment of durability performance. Side [8, 9] and radial [10] impact tests are designed to simulate the collision with a concentrated obstacle. These tests replicate the most severe working conditions of the wheel.

Some automotive OEMs perform cash tests that are more severe and complex than the tests proposed in this research. For such crash tests the detailed description of wheel and tire structure disruption seem lacking. Our study shows how the problem could be formulated for future simulations.

Side and radial impact tests of automotive wheels are described either by international standards [8, 9], or by standardized test procedures directly defined by vehicle manufacturers, such as the AK-LH 08 test procedures for vehicle wheels of German automotive manufacturers [10]. In the tests, the wheel is constrained to a supporting structure and a striker hits either the side or the tread of the tyre. The mass of the striker and the falling height depend on the required impact energy, function of the wheel size. Wheel cracks and deformations are measured after the tests and must remain under specified thresholds. Such tests, being destructive, are quite expensive and time consuming. A correct design of the wheel can minimize the manufacturer's time and costs if the radial impact test is passed at the first attempt. For this reason, a mathematical model able to correctly simulate the radial impact test can be a valuable tool for wheel design.

The side impact test is described in ISO and SAE standards [8, 9]. The

wheel is constrained to a hub fixture sloped at 13 degrees with respect to the horizontal plane. A flat striker, of prescribed mass, falls and hits the outer rim flange. The wheel has to withstand the load without fractures at the central part of the wheel or sudden air losses. The wheel is considered to have failed the test if any of the following conditions occurs:

- Visible fractures penetrate through a section of the centre member of the wheel assembly

- The centre member separates from the rim

- The tyre losses all air pressure within 1 minute

In the radial impact test [10] the wheel is fixed to a supporting structure in vertical position and a wedge-shaped striker falls on the tyre tread. The mass of the striker and the falling height depend on the required impact energy, function of the wheel size. Two impact energy levels (namely a low and high level) are prescribed from the standard, the acceptance criteria are the following:

- For the low energy level, a maximum residual deformation of 2.5 mm at the inboard rim flange is allowed

- For the high impact energy level, cracks are allowed at the wheel rim along a maximum of 25 % of the wheel circumference

Due to the complexity of the physical phenomena related to the radial impact test, a finite-element based model is the only practical choice for simulation. Finite element models of the side impact test can be found in the literature [11, 12, 13, 14, 15, 16, 17]. In these papers, complete nonlinear models of tyre and wheel have been implemented. The actual structure of the tyre has been modelled. A Mooney-Rivlin model [18, 19] has been employed for describing the tyre rubber material and the complete nonlinear elasto-plastic constitutive law of the aluminium material of the wheel has been included. In [12, 16] strain gauges were placed on the wheel to measure the local strain field during an impact test and for validating the numerical model. In [14] also the material

3

inhomogeneity of the wheel was considered. Different stress/strain properties have been assigned to hub, spoke and rim regions of the wheel based on experimental tests made on specimens extracted from the corresponding areas. In the same paper, the authors developed also a simplified version of the model by eliminating the tyre portion to reduce the computational time. In the simplified model, the tyre contribution was introduced by reducing the impact energy of about 20%.

Referring to the radial impact test, to the authors' knowledge, very few references dealing with its simulation are available in the literature. In [15] a 90-degree impact test has been simulated by means of finite elements. In this case a flat striker hitting on the internal portion of the tyre tread has been simulated. Results have been analysed and compared with experiments. Tan et al. [20, 21] conducted an experimental campaign to assess the influence of a set of parameters on the radial impact behaviour of a front motorcycle tyre-wheel assembly. On the base of the collected data, the authors developed an empirical model aimed at predicting the wheel response.

In the present paper, a procedure to develop a finite element model of a radial impact test is presented. On the basis of the model presented in [22], the main simulation issues are discussed and some experimental tests for the calibration of the model are presented. An experimental campaign concerning five different wheel types is reported for a comprehensive validation of the modelling approach. The resulting model is able to correctly simulate the test, by predicting with a good accuracy wheel cracks and deformations.

The paper is organized as follows. Firstly the radial impact test is presented and the differences with the side impact test are highlighted. Then, the modelling procedure is presented with particular attention to the model of the tyre which plays a crucial role in the computation of the forces acting on the wheel. Finally, the experimental validation is described.
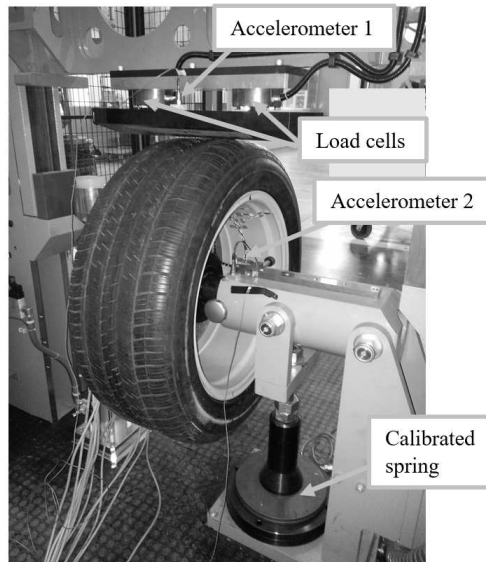
2. Radial impact test

Radial impact test [10] and side impact test [8, 9] are designed to test two different, and critical, loading conditions for the wheel. In case of side impact test, the aim of the test is to provide a load representing an accidental impact of the side of the wheel against a lateral obstacle such as a curb. In this case, the striker impacts both the side of the wheel rim and the side of the tyre. Most of the impact force, up to 80% according to [14], is applied directly to the wheel. The most critical zones of the wheel are the spokes and the rim near the impact location.

Conversely, in the radial impact test the striker impacts exclusively the tread of the tyre. In fact, the test is designed to simulate the impact due to a sharp vertical bump in the road. In this situation, the impact force is completely transmitted by the tyre to the wheel rim. The model of the tyre plays a critical role, particularly in case of high impact energy where the tyre sidewalls are completely folded. In this test, the most critical zone of the wheel is the rim, while the stress on the spokes is relatively low.

The typical set up of the radial impact test is shown in Fig 1(a). The wheel is fixed to a supporting structure and the striker is dropped from a specified height. The profile and main dimensions of the striker are sketched in Fig 1(b). The mass of the striker and the dropping height define the energy level of the test. The energy level is prescribed by the standards as function of the wheel and tyre dimensions. The supporting structure of the wheel is connected to the ground by a calibrated spring. The stiffness of the spring is quite important as influences the maximum impact force. The spring stiffness of the considered test rig is 85 kN/mm.

The test rig is usually instrumented by load cells to measure the impact force at the striker and a velocity sensor to measure the velocity of the striker at the impact (and thus the kinetic energy). In the set up of Fig 1(a) two additional accelerometers are located on the striker and on the supporting structure for model validation purposes.

(a)

(b)
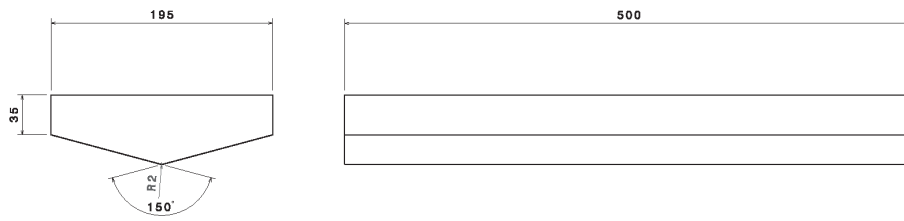
Figure 1: Radial impact test. (a) Test set up. (b) Main dimensions (expressed in mm) of the striker. (c) Maximum deflection of the tyre.
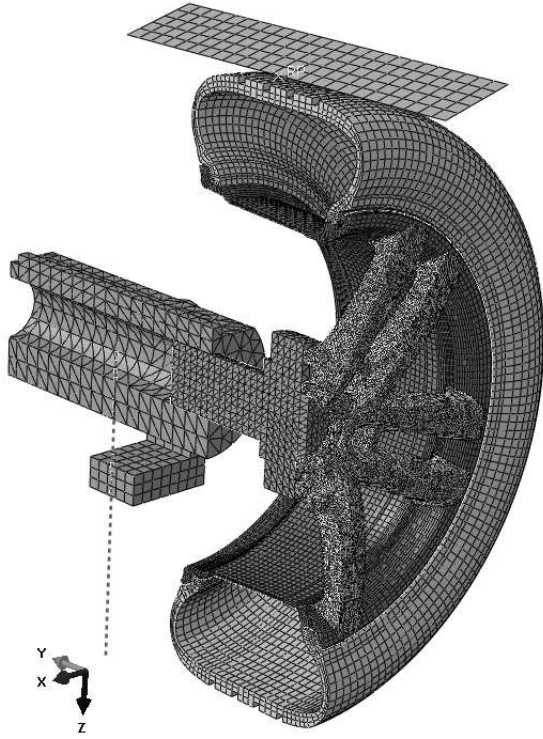
Figure 2: Finite element model of the radial impact test rig.

In Fig 1(c), the instant of the maximum penetration of the striker is depicted. When the maximum penetration is reached, the tyre sidewalls are completely folded. The wheel rim flange is plastically deformed and the interaction force between tyre and rim is very complex. Since the great majority of the plastic deformations happens in this condition and the residual deformations of the rim are the actual output of the test, the correct modelling of the tyre characteristics also in this condition is very important. In the following, a simple but effective procedure to identify the parameters of a suitable tyre model is presented.

3. Numerical model development

In this section the finite element model for the simulation of the radial impact test is presented. The model is developed by means of the commercial software

"ABAQUS Explicit 6.12" [23]. The model comprises wheel, tyre, striker and wheel fixture as depicted in Fig. 2.

3.1. Tyre model

The finite element model of the impact test rig is aimed to the study of the wheel permanent deformation and not to understand the behaviour of the tyre. A detailed model of the tyre is out of the purpose of this model, however the tyre model we propose is quite refined. The tyre model must be simple in order to devote the less possible time to its tuning, but able to get the radial force-deflection characteristic of the tyre with sufficient accuracy.

The tyre model considered in this paper is a finite element model of the tyre with a simplified structure. The material parameters are taken from the literature and tuned by simple experimental tests.

The considered structure of the tyre is modelled as depicted in Fig. 3. The geometrical dimension of the cross section of the tyre plays a crucial role in the folding phase of the deformation. To have an accurate description of the dimensions, the actual cross section of the tyre was measured with a "FARO" 3D measuring arm and imported into the finite element software.

Different rubber compounds can be found in different regions of a tyre. In the considered model, only two rubber materials are considered, one for tyre sidewalls and undertread and one for the tread. The two rubber compounds are modelled by hyperelastic materials described by a Mooney-Rivlin constitutive law. The Mooney-Rivlin coefficients are adapted from [18] and reported in Tab. 1, the strain rate dependency was not accounted in the numerical simulation [24, 11, 13]. The steel beads are modelled by an isotropic material. The tyre plies are modelled with layers of equally-spaced fibres embedded in the tyre carcass. A 90-degree ply is embedded in the whole carcass. A symmetric ±20-degree steel belt is added in the tyre tread as shown in Fig. 3. The material parameters and the geometric properties of the plies of a 265/50 R19 radial tyre are summarized in Tab. 1 and Tab. 2 respectively.

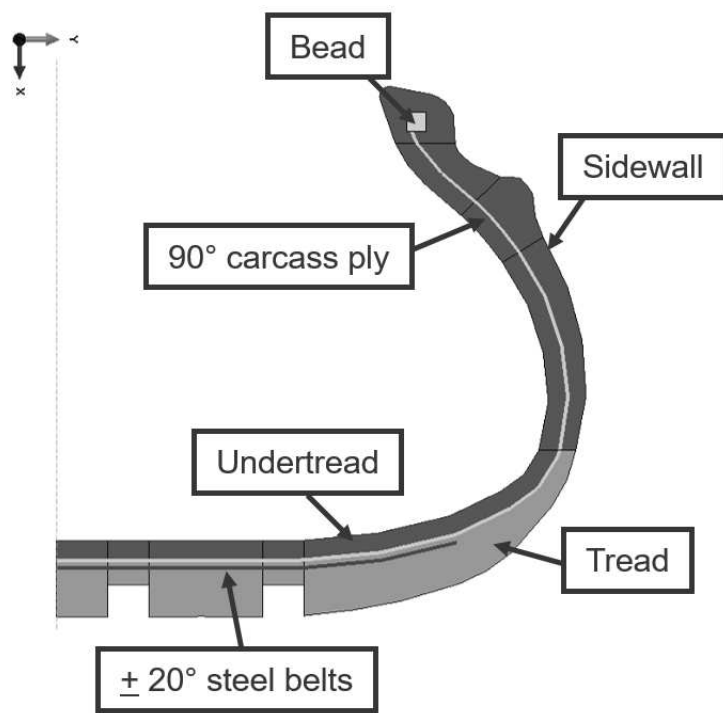In the numerical model, the stiffening effect induced by the tyre inflation

8

Bead

Sidewall

90° carcass ply

Undertread

Tread

± 20° steel belts

Figure 3: Tyre structure considered in the model.

Table 1: Material properties of a 265/50 R19 radial tyre

	Material type	Parameters
Steel	Linear elastic	$E = 210GPa, \nu = 0.3, \rho = 7800\frac{kg}{m^3}$
Nylon	Linear elastic	$E = 3.4GPa, \nu = 0.3, \rho = 1140\frac{kg}{m^3}$
Sidewall/undertread	Mooney-Rivlin	$C_{10} = 0.1MPa, C_{01} = 0.4MPa, \rho = 1100\frac{kg}{m^3}$
Tread	Mooney-Rivlin	$C_{10} = 0.14MPa, C_{01} = 1.8MPa, \rho = 1100\frac{kg}{m^3}$

Table 2: Geometric properties of the plies

	Wire spacing mm	Wire cross section mm^2
90 degree ply	1	0.4
± 20 degree belts	1	0.2

pressure is introduced by applying a uniform pressure on the inner side of the tyre surface and on the wheel rim. The inflation pressure is applied separately in an initial simulation step, the other loads are then applied in subsequent simulation steps.

The tyre model is tuned by means of experimental static tests on an actual tyre. The force/displacement curve of the tyre is measured at three different inflation pressures. The experimental tests have been conducted at the LaST (Laboratory for the Safety of Transportations) laboratory of Politecnico di Milano. The tyre/wheel assembly is fixed to a supporting structure as depicted in Fig. 4.

The vertical load is applied by means of the sliding platform shown in Fig. 4 moved by a hydraulic actuator. The horizontal plate on top of the platform is in contact with the tyre tread. The plate is guided by two vertical rails and
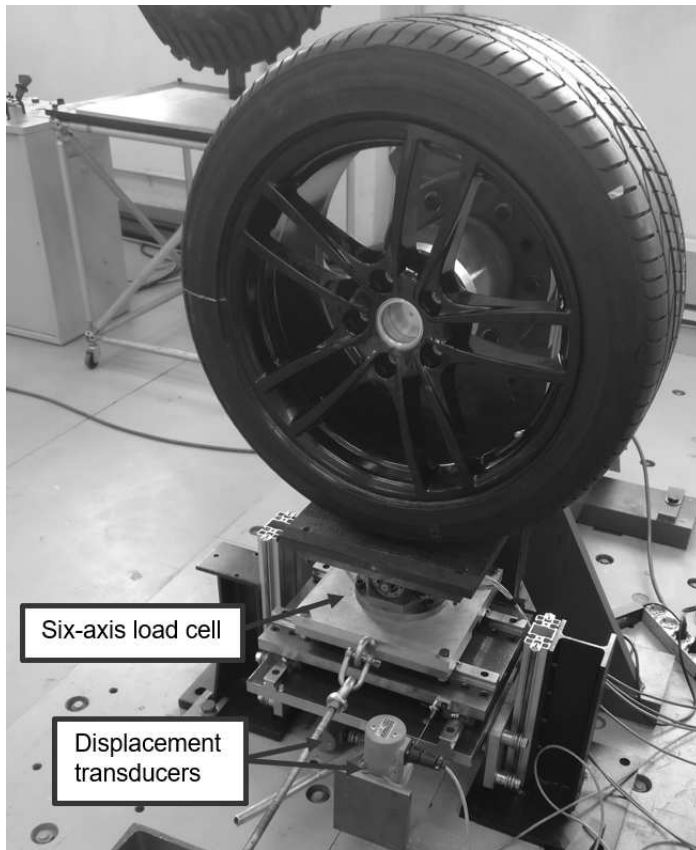
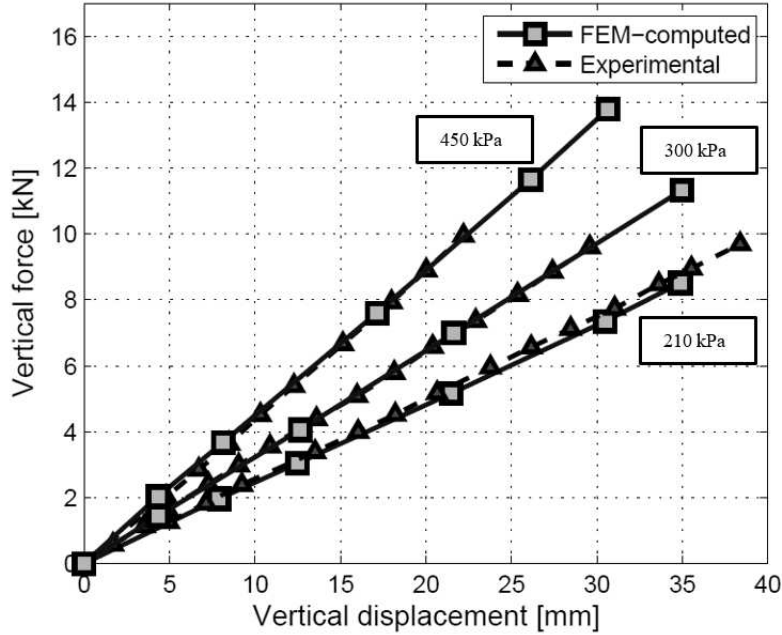Figure 4: Test bench for the measurement of tyre stiffness.

Figure 5: Numerical and Experimental force/displacement curves of a 265/50 R19 radial tyre at three different inflation pressures.

is mounted on a xy table that allows lateral and longitudinal displacements when the vertical load is applied. By such a test bench, any combination of vertical, lateral and longitudinal load can be applied to the wheel and different wheel types can be tested [2, 25]. Applied forces are measured by means of a six-axis load cell designed and realized at Politecnico di Milano [26]. The load cell is mounted immediately below the horizontal plate in contact with the tyre tread. The displacement of the loading platform along the vertical direction is measured by means of a displacement transducer shown in Fig. 4.

The measured force/displacement curves are compared with the ones obtained from the finite element model. The comparison between the experimental and numerical results is shown in Fig. 5. Tab. 3 summarizes the comparison in terms of vertical stiffness. The agreement between experimental and numerical data is good, with a maximum difference of 5% on the tyre vertical stiffness.

In the impact test, the tyre is hit by a wedge-shaped intruder. To verify

Table 3: 265/50 R19 radial tyre vertical stiffness at several inflation pressures.

Pressure [kPa]	Stiffness (measured) $\left[\frac{N}{m}\right]$	Stiffness (computed) $\left[\frac{N}{m}\right]$	Difference [%]
210	250000	236000	5.6
300	323000	325000	0.6
450	449000	432000	3.8

the effectiveness of the identified tyre parameters, an experimental static test with the actual wedge-shaped intruder has been conducted as shown in Fig. 6a. The wheel was mounted on the radial impact test bench and a quasi-static load has been applied to the wedge-shaped intruder. The test was performed at a zero inflation pressure to explore the complete range of deformation of the tyre structure without reaching large values of the vertical force that could damage the wheel rim. The measured force/displacement curve is shown in Fig. 6b and compared with a numerical simulation. The curves exhibit an almost linear behaviour for the first part of the vertical stroke of the intruder, then, after approximately 70 mm, the large deformation of the tyre cross section forces the inner surfaces of the tyre sidewalls to get in contact causing a rapid increase of the vertical stiffness. For this test the matching between the curves is good, with a difference below 5 %.

Tyre damping is introduced in the simulation through a Rayleigh model. In this model, the damping matrix of a structure is approximated as a linear combination of stiffness and mass matrices [27]:

$$\mathbf{C} = \alpha\mathbf{M} + \beta\mathbf{K} \tag{1}$$

where $\mathbf{M}, \mathbf{C}$ and $\mathbf{K}$ are mass, damping and stiffness matrices respectively, while α and β are the two Rayleigh's coefficients. The damping ratio ζ_i referring to the i_{th} eigenmode can be related to the modal angular frequency through the following relationship

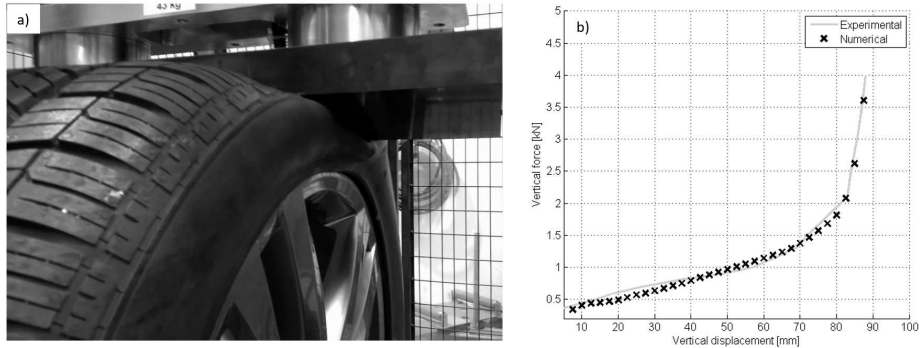$$\zeta_i = \frac{\alpha}{2\omega_i} + \frac{\beta\omega_i}{2} \tag{2}$$

13

Figure 6: a) static stiffness test realized with the wedge-shaped intruder b) comparison of numerical (cross markers) and experimental (solid line) force/displacement curves of a non-inflated 265/50 R19 tyre.

where ω_i is the angular frequency of the considered eigenmode. The two Raileigh's coefficients α and β are obtained from experimental modal tests on the actual tyre [28, 29, 30]. The frequency response functions (FRF) of the tyre tread and sidewall were measured by means of two PCB 20G single-axis capacitive accelerometers and a PCB 086D20 impulse force hammer. The accelerometers were located on the tyre tread and on the sidewall as shown in Fig. 7. From the impact hammer and accelerometer signals, the measured FRFs of the tread and the sidewall are computed and shown in Fig. 8.

The FRF of the tread is cut at a frequency of 270 Hz, for the sidewall the cut-off frequency is set to 140 Hz. A threshold of 20 dB attenuation of the spectrum of the input signal of the hammer has been considered to set the cut-off frequency. The damping ratio of each eigenmode has been estimated by means of the half-power bandwidth method [27] and reported in Tab. 4.

The Rayleigh's coefficients are then identified from the measured damping ratios and frequencies by means of a least-squares fitting on eq. 2. Fig. 9 depicts the fitting related to the tyre tread.

The identified parameters are shown in Tab. 5 for tread and sidewall respectively.

14

Figure 7: Accelerometers on the tyre tread (above) and sidewall (below).
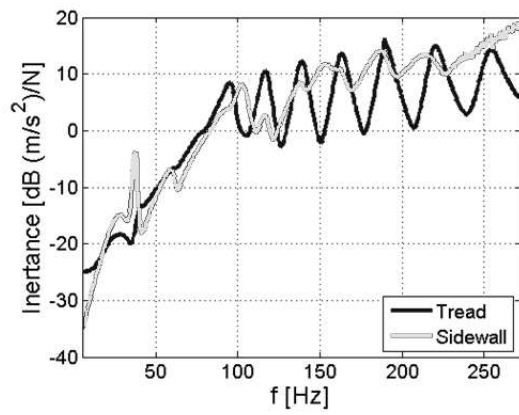

Figure 8: Frequency Response Function of the tyre tread and sidewall. Tyre pressure 230 kPa.

Table 4: Eigenfrequencies and damping ratios of the tyre tread and sidewall - 265/50 R19 radial tyre.

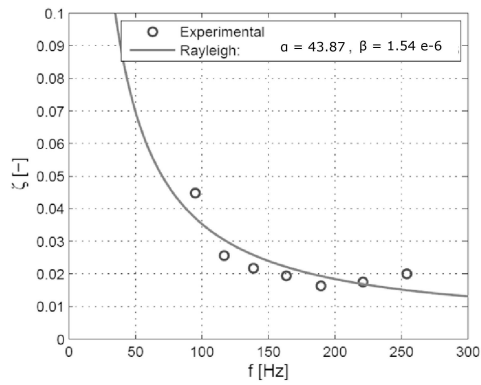| Frequency [Hz]	Damping ratio [%]
Tread	
95	4.48
117	2.56
139	2.17
164	1.94
190	1.63
221	1.75
254	2.00
Sidewall	
37	2.16
102	4.17

Figure 9: Experimental (circles) and interpolated (solid line) damping ratio of the tyre tread - 265/50 R19 radial tyre.

Table 5: Identified Rayleigh's coefficients for the tread and the sidewall - 265/50 R19 radial tyre.

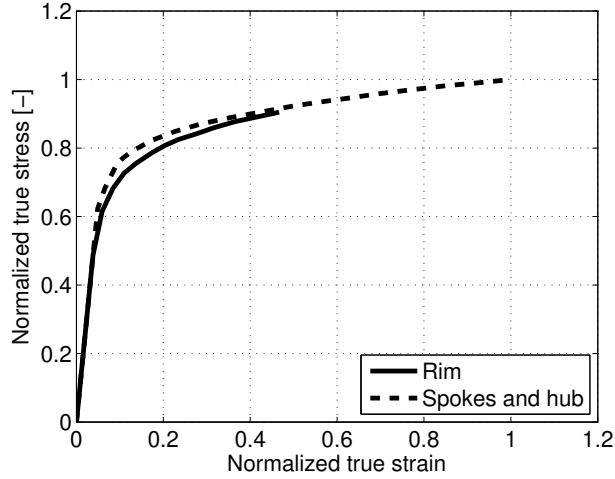|	α	β
Tread	43.9	$1.5e-6$
Sidewall	3.5	$1.2e-4$

Figure 10: Material constitutive laws employed for the rim region (solid line) and for the spokes/hub region (dashed line). The two curves are normalized over the same values

.

3.2. Wheel model

The A356 T6 aluminium alloy wheel is modelled with an isotropic material. Dealing with high deformations, elasto-plastic material behaviour is considered. The wheel material inhomogeneities, due to different cooling rates in the different zones of the wheel, are considered in the numerical model [14]. Specimens have been extracted from different locations of the wheel and used for the characterization of the material [1]. Two distinct material constitutive curves are considered for the wheel rim and the wheel spokes (and central hub). The two material constitutive laws are reported in Fig. 10.

As is evident from Fig. 10, the spoke region is characterized by a more

ductile behaviour of the material which exibits a more than double elongation at failure than the material of the rim region.

3.3. Striker and supporting structure model

The striker is modelled as a wedge-shaped rigid surface with the same profile described in the test standard. A concentrated mass is assigned to the rigid surface. The value of the mass depends on the amount of energy required by the test. The edge of the striker is inclined of an angle of 1 degree with respect to the tread surface of the tyre as required from the test standard.

The hub and the supporting structure are considered as rigid bodies. By this constraint, the computational time is greatly reduced while the inertial effects of the structure are considered.

3.4. Mesh and boundary constraints

Different interactions and boundary constraints are defined on the components of the model as follows (see Fig. 11).

- Symmetry constraint at the middle surface.

- Frictional contact constraints at the interface between tyre and wheel rim, friction coefficient equal to 0.5 [31].

- The wheel is rigidly connected to the supporting structure.

- The other end of the supporting structure is connected to the ground by a hinge constraint.

- The central part of the supporting structure is connected to the ground by means of an axial spring with stiffness equal to 85 kN/mm (42.5 kN/mm in the half model).

Referring to the mesh of the model, tyre and wheel rim are discretized with linear 8-noded brick elements, while for spokes and central hub linear tetrahedrons are employed. Details of the finite element mesh of one of the simulated wheels are reported in Tab. 6.
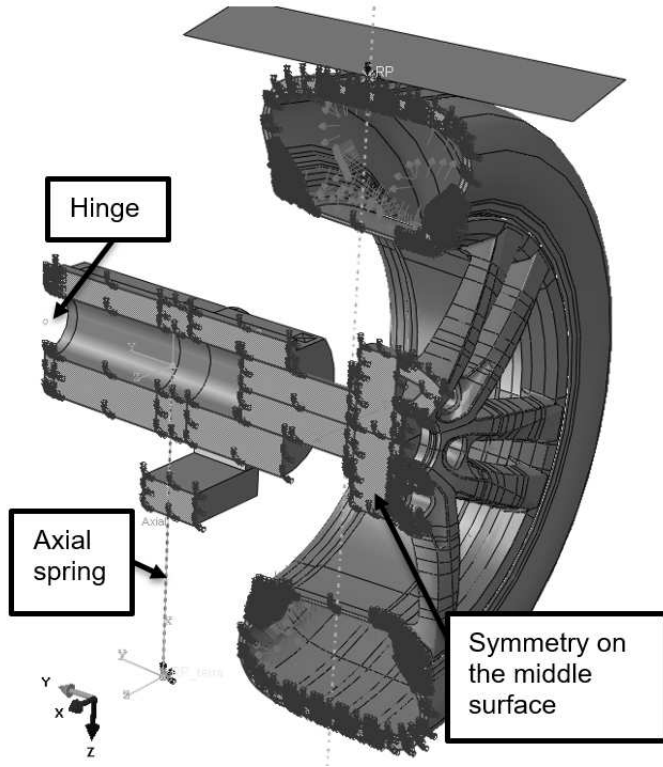
Figure 11: Constraint scheme of the model.

Table 6: Details of the finite element mesh of one of the simulated wheels.

	Element type	Typical element size[mm]	# elements [s]
Tyre tread	C3D8	6x7x13	5518
Tyre sidewall/undertread	C3D8	3x10x11	14261
Body ply and steel belts	SFM3D4	10x13	5607
Tyre beads	C3D8	3x3x8	712
Wheel rim	C3D8	2x7x7	20140
Spokes	C3D4	4x4x4	271174

19

Great efforts have been devoted to obtain a very regular mesh without distorted elements. In fact, when using an explicit solver, mesh quality greatly influences the minimum time step for integration and, as a consequence, the computational time. For this reason, wheel rim and spokes have been meshed separately and then constrained to reconstruct the continuity of the wheel. By this choice, stresses in the interface regions between rim and spokes are poorly approximated. However, this is not an issue in the present analysis since it is well known that the region of interest for stresses is in the wheel rim near the impact area, sufficiently distant from the spokes.

3.5. Simulation strategy

The numerical simulation is divided in two steps, namely:

- Tyre inflation

- Impact simulation

In the first step the tyre is gradually inflated at the nominal pressure. The tyre inflation pressure is introduced by adding a uniform pressure on the internal surface of the tyre and on the wheel rim, contact interactions are imposed at the tire/rim interface. The numerical solution is carried out by means of an implicit nonlinear solver, the large displacements elasticity theory is adopted. Fig. 12 shows an example of tyre profile before and after the inflation step, in the picture the different portions of the tyre structure are highlighted. The solution obtained from the first step is used as initial condition for the subsequent simulation of the radial impact. An initial velocity is prescribed to the striker and the radial impact test is simulated. An explicit solver is employed for this step. The time period of the simulation step has been set wide enough to allow a complete rebound of the striker and ensure elastic recovery of the rim after the impact. Due to the large deformation of the tyre during this step, a general contact option is employed to detect the surfaces in contact during the simulation. Fig. 13 depicts an example of deformed tyre and wheel rim at different simulation time instants.
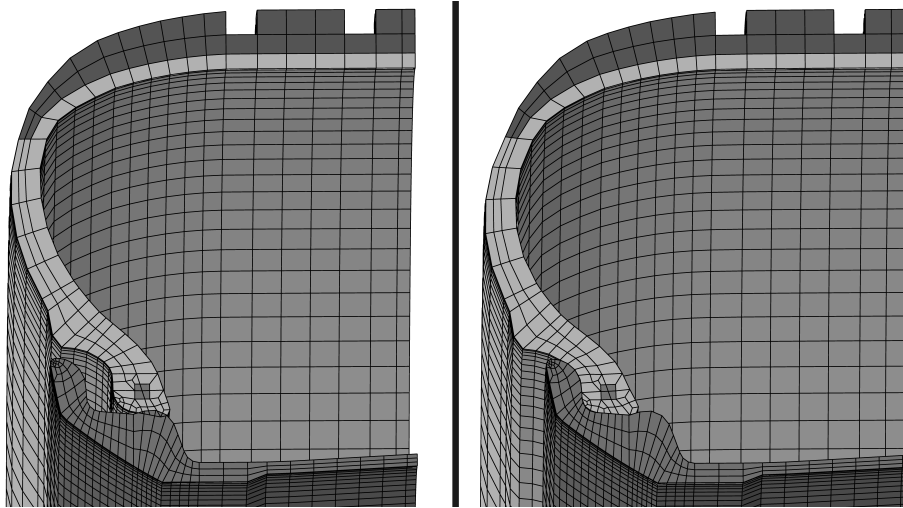
Figure 12: Undeformed (left) and deformed (right) tyre cross section after the inflation step - 265/50 R19 radial tyre, the different portions of the tyre structure are shown with different colors

.

The variation of the inflation pressure induced by the change of the volume of the tyre air cavity during its deformation is neglected in order to reduce the complexity of the numerical model. An explicit solver is employed for this step.

Tyre blowout is a typical failure mechanism that involves pneumatic tyres subjected to severe impact conditions [32]. Such a failure can be caused either by the rupture of the tyre structure, or by a debeading process, that happens when the tyre bead is separated from the wheel rim allowing the air in the cavity to escape. Since the focus of the analysis is on the wheel and not on the tyre, no investigation on tyre failure mechanisms was conducted. Orengo et al. [33] proposed an effective way to model the tyre debeading process, which is always due to a transverse overload of the tyre sidewall. In the impact test modelled in this paper, being the load predominantly acting along the radial direction of the tyre, the debeading process is not a critical issue.
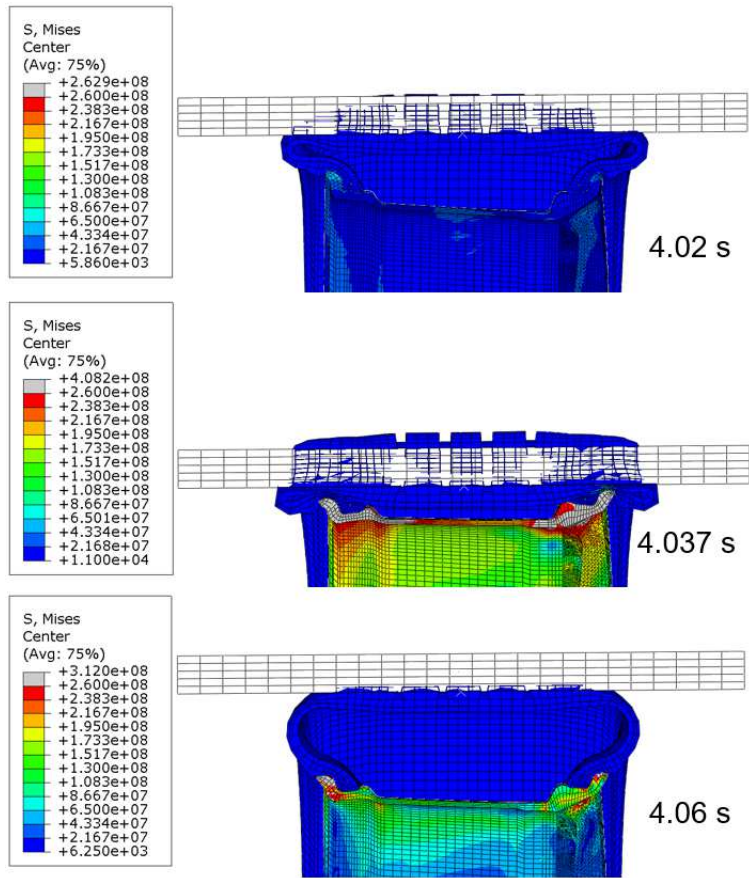
Figure 13: Von Mises stress at different simulation time instants - Impact energy 3380 J, 265/50 R19 radial tyre.

4. Experimental validation

The experimental validation of the model is performed in two stages. In the first stage, a wheel is instrumented by strain gauges and a comprehensive comparison between the results of the FE model and an actual impact test, repeated at two energy levels, is carried out. In the second stage, four additional wheel types are considered. The FE models of the wheel types are built following the steps described in Sect. 3. For each wheel type, from one to three impact tests, at two energy levels, are performed. The results of the impact tests, in terms of impact force and wheel deformation, are compared with the quantities predicted by the models. In this way, the procedure for the realization of the FE model is validated in relation to the impact test results and dispersion.

4.1. Instrumented wheel

A 19x8.5 wheel is instrumented with a set of resistive strain gauges located at the most stressed areas of the wheel. The wheel has a design with five twin spokes as can be seen from Fig. 2 and Fig. 11. Five 120-Ohm uniaxial strain gauges are placed on the front and backside of the spoke closest to the wedge impact region. Additionally, a tri-axial strain rosette is located near the connection between the spoke and the central hub. Fig. 14 shows the locations of the strain gauges on the spoke. Other six uniaxial strain gauges are located on the wheel rim. These strain gauges are equally spaced of an angle of 9 degrees, covering a sector of 36 degrees of the wheel rim as shown in Fig. 15. All the strain gauges are connected to a thermal compensator to reduce the negative effects associated with thermal gradients.

The impact tests are performed on the radial impact test bench shown in Fig1(a).

Signals, coming both from the wheel strain gauges and the test bench instrumentation, are acquired at a frequency of 25 kHz and filtered down to 500 Hz with a digital FIR (Finite Impulse Response) filter in post-processing stage. Additionally, after each test, the residual deformation of the rim on the inner side of the wheel is measured.
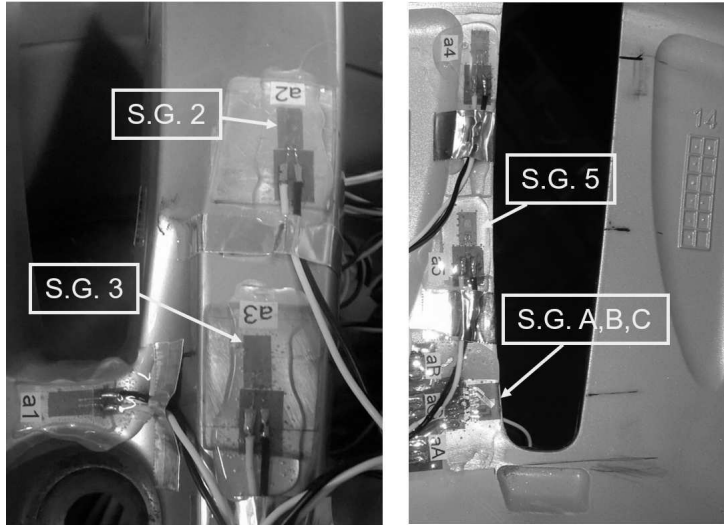
Figure 14: Strain gauges location on the wheel spoke.

Figure 15: Strain gauges location on the wheel rim.

Table 7: Energy levels tested for the Instrumented wheel.

Energy (nominal) [J]	Striker mass [kg]	Falling height [m]	Impact velocity (measured) [m/s]	Energy (measured) [J]
700	150	0.476	2.9	631
3500	260	1.372	5.1	3381

The wheel is mounted on the support so that the impact area is concentrated between two consecutive spokes.

Two different energy levels are tested, namely 700 Joule and 3500 Joule. The parameters related to the two tests are reported in Tab. 7. In the 700 Joule test the mass of the striker is 150 kg, falling from a height of 476 mm, while in the 3500 Joule test the mass is 260 kg and the falling height is 1372 mm. The velocity of the striker when impacting the tyre is recorded so that the actual impact energy of the test can be measured (see Tab. 7). For the validation of the model, the two impact tests have been simulated by using as input the measured velocities.

The measured quantities are compared with the simulated ones for both the 700 and 3500 Joule tests.

Fig. 16 shows the comparison between the measured and computed accelerations of the striker for the 700 Joule (Fig. 16a) and 3500 Joule (Fig. 16b) test respectively.

Referring to the 700 Joule test, the agreement between the numerical and experimental data is excellent, with a difference of less than 1% on the maximum acceleration. In the 3500 Joule test, the model seems to overestimate the acceleration peak.

The displacement of the supporting structure is obtained by integrating the acceleration time history measured by the second accelerometer. A comparison
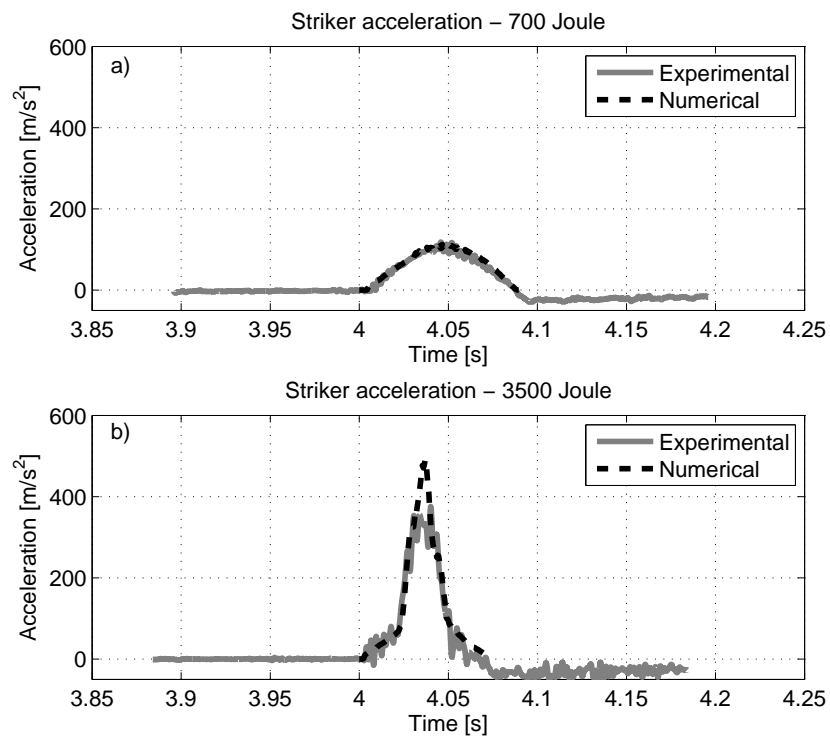
Figure 16: Measured (gray) and simulated (dashed black) acceleration of the striker for the 700 Joule (a) and 3500 Joule (b) tests.
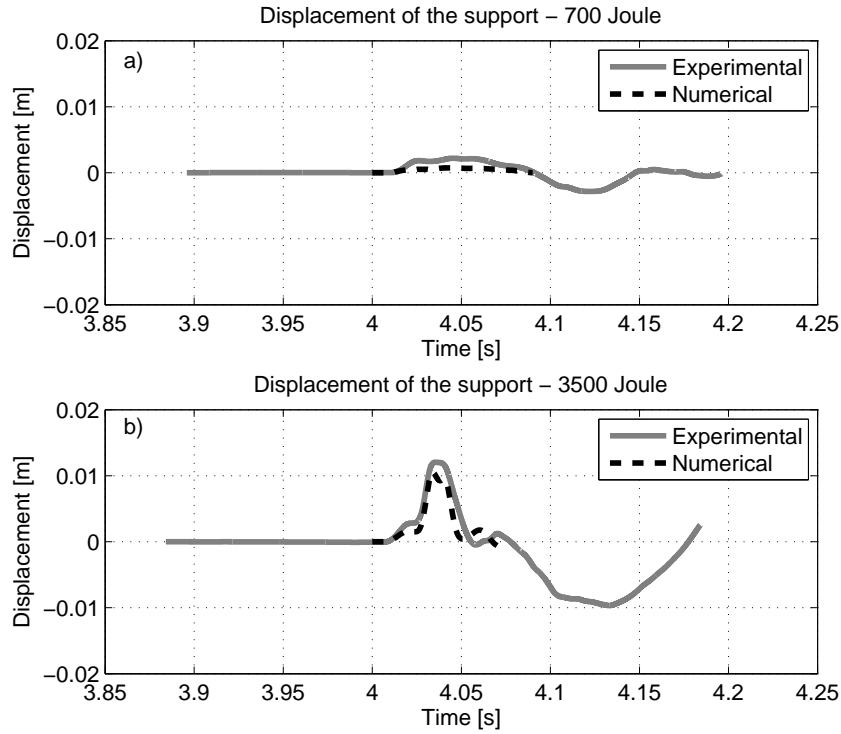
Figure 17: Measured (gray) and simulated (dashed black) displacement of the supporting structure for the 700 Joule (a) and 3500 Joule (b) test.

with the numerical simulation is shown in Fig. 17a and 17b for the 700 Joule and 3500 Joule test respectively. A difference of about 12 % is obtained for the 3500 Joule test, where a peak of 12 mm is reached on the supporting structure. For the 700 Joule test, the maximum displacement of the support is nearly 2 mm and a larger discrepancy with the numerical simulation is experienced.

In Fig. 18 the measured and simulated impact forces are depicted for the two energy levels. For the 3500 Joule the error on the force peak is about 20%, mainly affected by the difference in the acceleration time history of Fig. 16b.

Fig. 19 shows the comparison between the measured and computed strain levels at the wheel spokes for the two considered energy levels (top: 700 Joule test, bottom: 3500 Joule test). In this case a good matching has been obtained
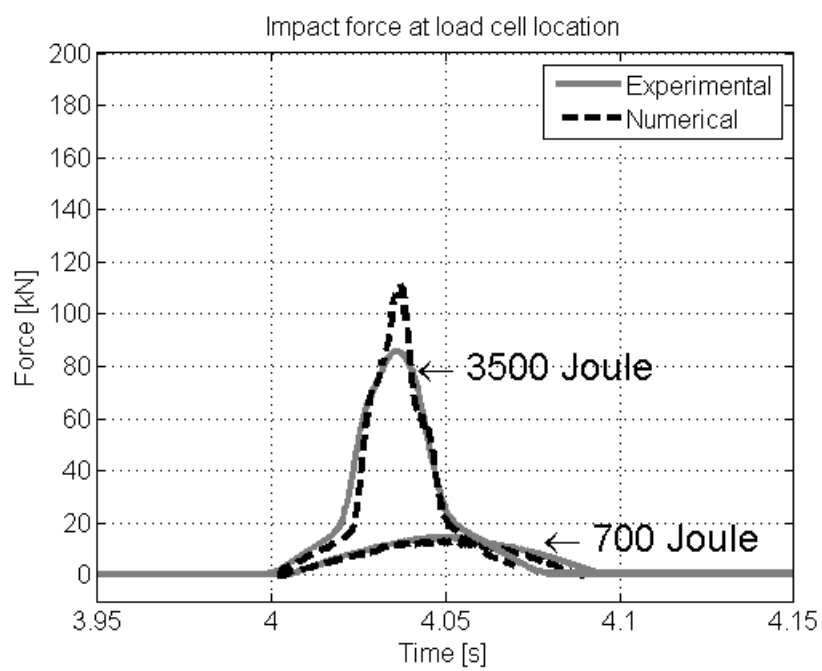
Figure 18: Measured (gray) and simulated (dashed black) impact force.

28

for both tests.

In Fig. 20 the principal stress calculated from the signals of the strain rosette is depicted and compared with the FEM results (top: 700 Joule test, bottom: 3500 Joule test). Again experimental and numerical results are closer for the 700 Joule test. For the 3500 Joule test a higher difference occurs at the stress peak, which could be related to the difference in the measured and computed impact force of Fig. 18.

Finally, the signals of the strain gauges located on the wheel rim are depicted in Fig. 21 (top: 700 Joule test, bottom: 3500 Joule test). For the high energy test (3500 Joule) a residual deformation remains after the impact. The numerical model is able to compute the residual deformation with a good accuracy. In this case a difference below 14% can be seen both at the maximum strain and on the residual strain.

A good agreement on the residual deformation of the internal rim flange has been obtained too, as shown in Fig. 22. The maximum measured and simulated residual deformations at the internal rim flange differ of less than 10%. Moreover, also the deformed shapes of the rim are very similar as shown in Fig. 22.

4.2. Extended validation

In this section, four additional wheel types are considered to validate the modeling procedure proposed in the paper. The main characteristics of the four considered wheel types, along with the characteristics of the instrumented wheel considered in Sect. 4.1, are reported in Table 8. The whole set of five wheel types is composed by wheels with very different geometries. Moreover, each of the selected wheel type is equipped with a different tyre. In total, five different wheel types have been selected for the validation and are denoted as: Instrumented wheel (Sect. 4.1), W1, W2, W3 and W4. As shown in Tab. 8, the diameter of the wheels ranges from 19” to 20”, while the rim width ranges from 8.5” to 11”. In one case (wheel W4), a run-flat tyre is mounted on the rim.

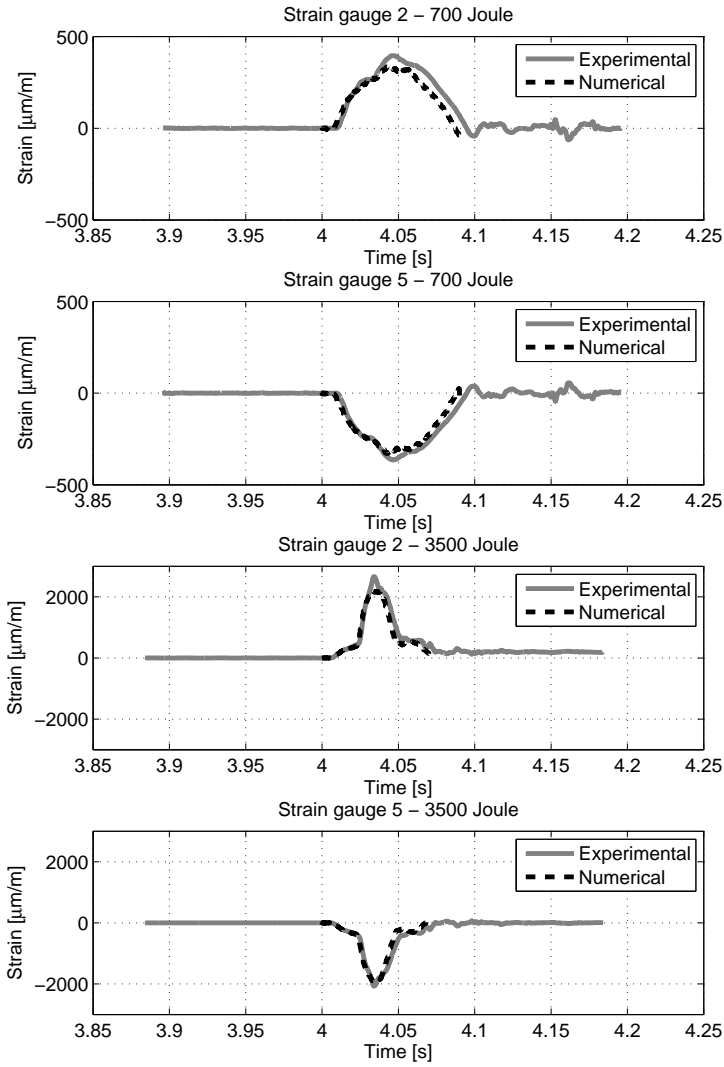The impact tests have been performed on the same test rig of Sect. 4.1 (Fig.

Figure 19: Measured (gray) and simulated (dashed black) strain signals of strain gauges 2 and 5 for the two energy levels tested.
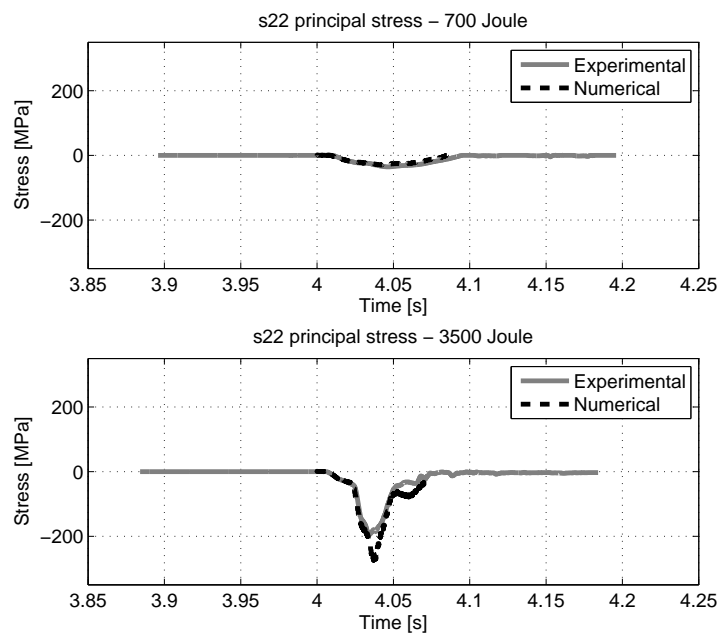
Figure 20: Experimental (gray) and simulated (dashed black) principal stress measured by the strain rosette.
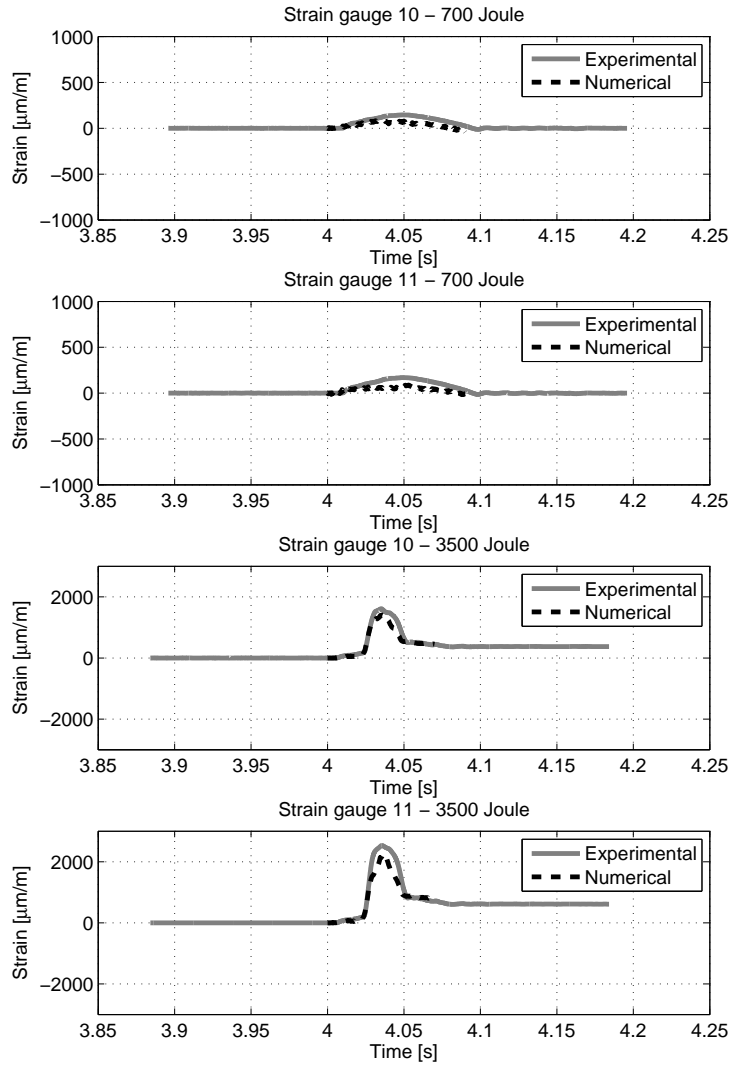
Figure 21: Measured (gray) and simulated (dashed black) signals of strain gauges 10 and 11 for the two energy levels tested.
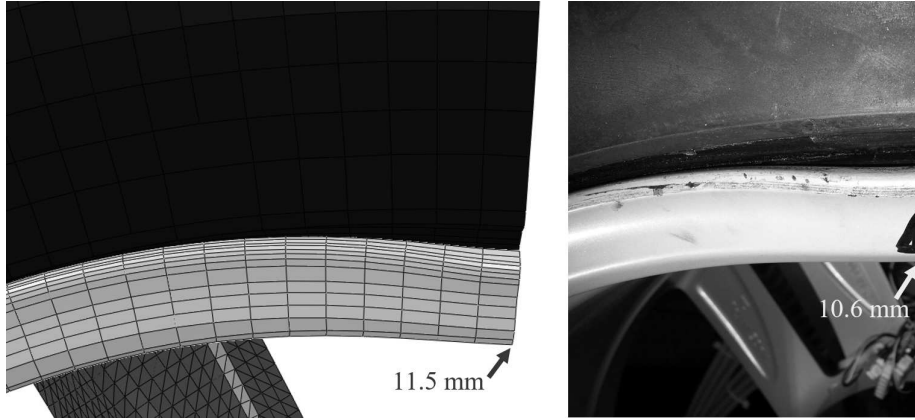
Figure 22: FEM-computed (left) and actual (right) residual deformation of the internal rim flange after the 3500 Joule test.

Table 8: Main features of the tested wheel types and relative tyres.

Wheel name	Wheel mass [kg]	Nominal load [N]	Wheel diameter [mm (in)]	Rim width [mm (in)]	Tyre size
Instrumented wheel	14.8	8000	483 (19)	216 (8.5)	265/50 R19
W1	13	8300	508 (20)	267 (10.5)	305/40 R20
W2	10.8	4800	508 (20)	254 (10)	265/35 R20
W3	13.5	7200	483 (19)	216 (8.5)	255/45 R19
W4	17.5	8800	508 (20)	279 (11)	315/35 R20 Run-flat

1(a)) at two impact energy levels for each wheel type, namely a low energy and a high energy level. In Table 9 the nominal values of the energy levels, the measured levels of energy and the number of repetitions are reported for each wheel type.

For each wheel type, a FE element model of the impact test has been realized following the procedure described in Sect. 3, the numerical models are shown in Fig. 23. In Table 10 the material parameters of the four wheel tyre types identified during the construction of the FE model are reported. Fig. 24 depicts the comparison of the simulated and experimental force/displacement curves

33

Table 9: Experimental tests performed on the selected wheel types.

Wheel type	Energy (low/high) [J]	#replicates
Instrumented wheel	630/3380	1
W1	970/3640 ±2%	2
W2	560/2100 ±2%	2
W3	840/3140 ±2%	3
W4	1035/3870	1

for the tyres mounted on wheels W1, W2, W3 and W4 at the nominal inflation pressure. By using the FE models, the low and high energy impact tests have been simulated for the considered wheel types. The time period of all the performed simulations has been set wide enough to allow a complete rebound of the striker and ensure elastic recovery of the rim after the impact.

In Fig. 25, the comparison between measured and simulated peak impact forces and residual displacements at the inner rim flange are reported for all the tested wheels, both for the low and high energy levels. Regarding the impact force (Fig. 25a), the comparison shows a good matching, with the discrepancy bounded within a 10% deviation for the majority of the tested wheels.

Regarding the residual displacements (Fig. 25b), in the low energy impact tests a very small amount of inelastic deformation remains after the test. For the high energy impact tests, wheels W1, W2 and W4 exhibit a good correlation. For wheel W3, a larger residual displacement has been measured at the inner flange with respect to the predicted one. In this case, the actual wheel showed cracks along the wheel rim. The damage mechanism is not modelled in the numerical simulation and the structural stiffness reduction caused by the opening of cracks is not considered, thus making the numerical model stiffer than the actual wheel. For this reason an additional simulation accounting for the damage mechanism (explained in paragraph 4.2.2) has been performed on wheel W3 showing a significant improvement in the correlation with experimen-
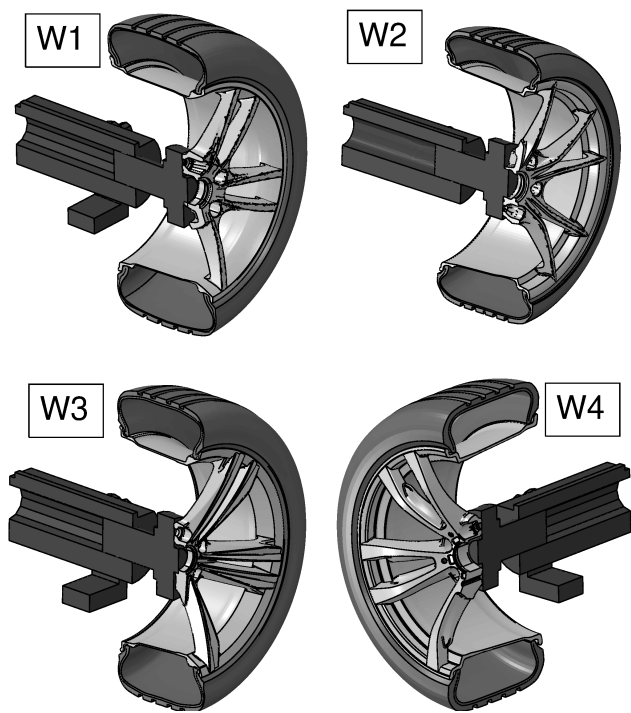
W1 W2

W3 W4

Figure 23: Finite element models of the four additional wheels considered for the validation.

Table 10: Identified material properties of the tyres mounted on wheels W1, W2, W3 and W4.

| Tyre size	Region	Material type	Parameters
305/40 R20	Sidewall/undertread	Mooney-Rivlin	$C_{10} = 0.15 MPa, C_{01} = 1.00 MPa$
	Tread	Mooney-Rivlin	$C_{10} = 0.14 MPa, C_{01} = 1.80 MPa$
265/35 R20	Sidewall/undertread	Mooney-Rivlin	$C_{10} = 0.10 MPa, C_{01} = 0.40 MPa$
	Tread	Mooney-Rivlin	$C_{10} = 0.14 MPa, C_{01} = 1.80 MPa$
255/45 R19	Sidewall/undertread	Mooney-Rivlin	$C_{10} = 0.10 MPa, C_{01} = 0.32 MPa$
	Tread	Mooney-Rivlin	$C_{10} = 0.11 MPa, C_{01} = 1.40 MPa$
315/35 R20 Run-flat	Sidewall/undertread	Mooney-Rivlin	$C_{10} = 0.14 MPa, C_{01} = 0.40 MPa$
	Tread	Mooney-Rivlin	$C_{10} = 0.14 MPa, C_{01} = 1.80 MPa$
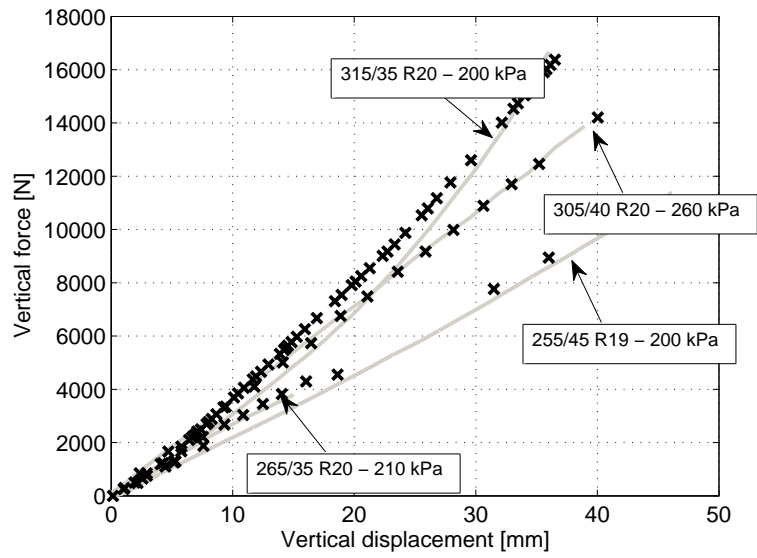
Figure 24: Comparison between experimental (solid grey) and numerical (cross markers) force/displacement curves for the tyres of wheels W1,W2,W3 and W4 at the nominal inflation pressure.
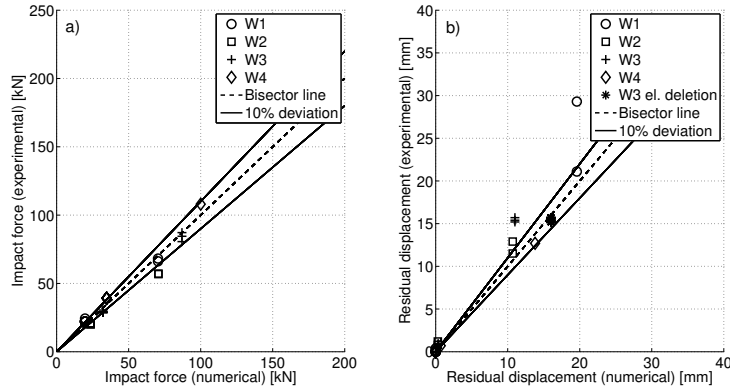
Figure 25: Comparison between numerical and experimental data for wheels W1, W2, W3 and W4 (both low and high energy impact test). a) Impact force. b) residual displacement at the inner rim flange.

tal data. The same situation holds for one replica of wheel W1, which showed a disruptive failure of the wheel rim that is responsible of the large difference with the numerical simulation.

In Fig. 26 the measured and simulated time histories of wheels W1, W2 and W3 during the high energy test are shown; for wheel W4 only information regarding the maximum impact force were available. The comparison shows that the shape of the numerical curve is slightly narrower than the measurements and exhibits a higher peak, denoting a stiffer behaviour that can be explained by the numerical simplification adopted for modelling the connection between the wheel and the ground support, where a perfectly rigid connection has been employed instead of modelling the bolted interface.

All the tested samples of wheel types W1 and W3 exhibited fractures along sectors of the wheel rim after the high energy test. As shown in Fig. 27, cracks appeared frequently at the area close to the outboard wheel hump and in one case near the outboard flange. Such failures are ductile fractures, in the following paragraphs (4.2.1 and 4.2.2) two different methods employed for damage prediction are discussed.
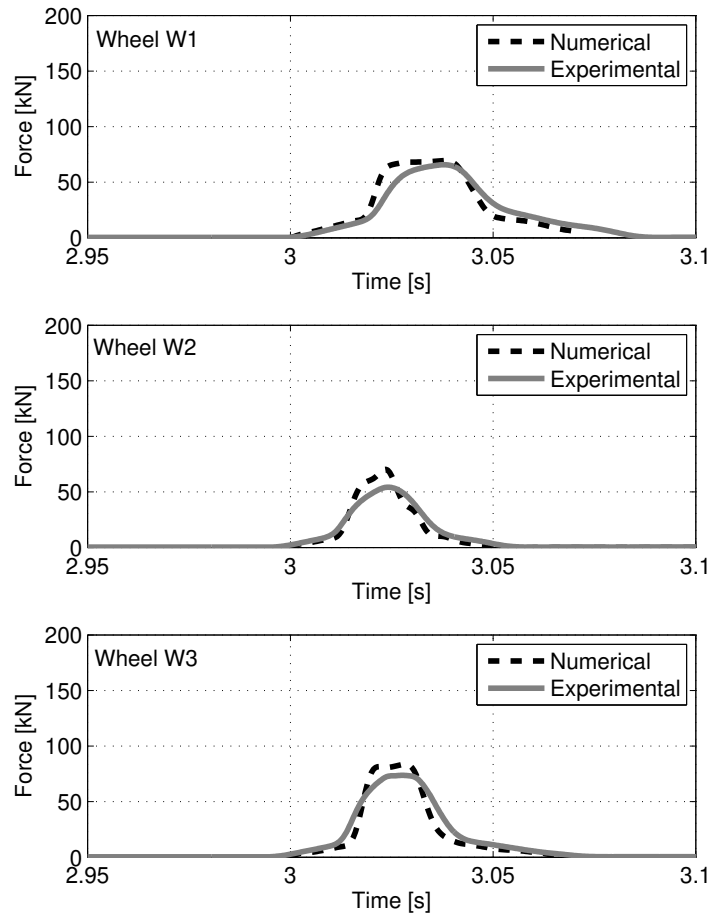
38

Figure 26: Comparison between numerical (dashed black) and experimental (solid grey) time histories of the impact force for wheels W1, W2 and W3 during the high energy impact test.
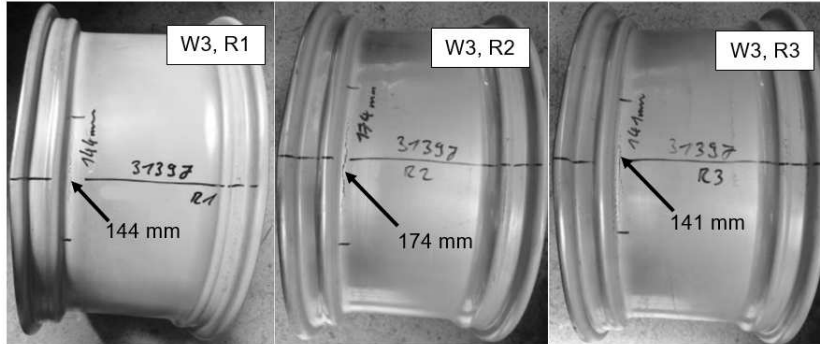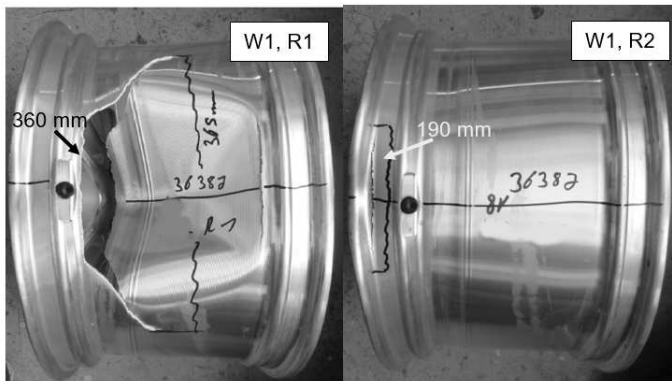
Figure 27: Pictures of wheels W1 (above) and W3 (below) after the high energy impact test.

4.2.1. Damage prediction through strain energy density

The total plastic work per unit of volume W_p has been considered as a failure index [12]. This quantity is defined as

$$W_p = \int_0^{\epsilon_f} \sigma_t d\epsilon_p \tag{3}$$

being ϵ_f, σ_t and ϵ_p the ultimate strain, the true stress and the plastic strain respectively. The plastic stress-strain relationship of the material has been interpolated by the Hollomon's equation

$$\sigma_t = K \left(\epsilon_p\right)^n \tag{4}$$

with K and n the material strength coefficient and the strain hardening exponent respectively.

By substituting eq. 4 in eq. 3 and computing the integral, the total plastic work per unit of volume can be expressed as

$$W_p = \int_0^{\epsilon_f} K \left(\epsilon_p\right)^n d\epsilon_p = \frac{\sigma_f \epsilon_f}{n+1} \tag{5}$$

where σ_f is the true stress at fracture. Eq. 5 provides the critical value of strain energy density for fracture. The limit W_p is obtained from tensile stress test performed in the different zones of the wheel.

Fig. 28 depicts the contour plot of the plastic strain energy density of the FE models of wheels W1 and W3. In the grey area, the estimated value exceeds the critical limit of the material and fractures are expected. As it can be observed, the numerical model confirms the experimental results of Fig. 27.

4.2.2. Damage prediction through Johnson-Cook damage model

Beside the strain energy density approach, a more recent and advanced fracture criterion has been employed to predict damage occurrence on the wheel. A wide number of failure criteria is available in the literature to describe fracture of ductile materials [34, 35]. These criteria identify a fracture locus defined as the general function in eq. 6

$$\epsilon_f = f\left(\eta\right) = f\left(\frac{\sigma_m}{\overline{\sigma}}\right) \tag{6}$$
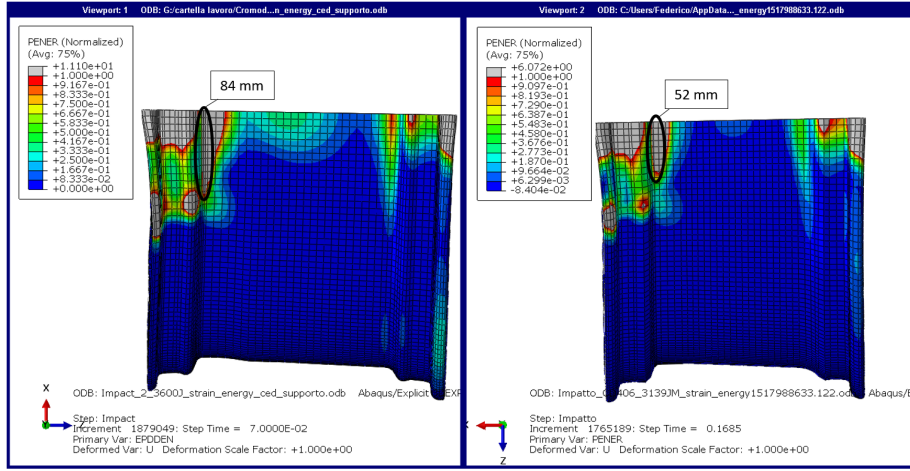
41

Figure 28: Contour plot of the (normalized) plastic strain energy density computed on the models of wheel W1 (left) and W3(right). In the grey area the material critical value is exceeded and fractures are expected, data are normalized on the material limit.

where ϵ_f is the effective plastic strain to fracture, while η is the stress triaxiality, defined as the ratio of the hydrostatic stress σ_m and the von Mises effective stress $\overline{\sigma}$. In particular, in this analysis, the Johnson-Cook fracture criterion has been employed, which relates ϵ_f and η through the exponential function in eq. 7 [36]

$$\epsilon_f = D_1 + D_2 \exp\left(D_3\eta\right) \tag{7}$$

where D_1, D_2 and D_3 are material constants, which can be identified by means of tensile tests on specimens with different geometry and related finite element simulations [37]. In this study, material parameters taken from [37] have been considered. To account for the more brittle behaviour of the wheel rim, parameters of the sand-molding A356 aluminum have been employed in this region of the wheel [38], while metal-molding parameters have been assigned to the more ductile region of the spokes and central hub. The Johnson-Cook parameters employed for the simulations are summarized in Tab. 11.

Element deletion has been included in the numerical models to simulate the

Table 11: Johnson-Cook damage parameters employed for numerical simulations. Data are taken from [37].

Region	D_1	D_2	D_3
Wheel rim	0	0.27	-2.9
Spokes and hub	0	0.65	-2.2

crack opening process. Numerical results of wheels W1 and W3 are depicted in Fig. 29, where the contour plot of the Johnson-Cook damage parameter [23] is shown for the two considered wheels. From the picture it can be observed that the damage mechanism of the wheels is well reproduced by numerical simulation. In particular, for wheel W3 both crack location and crack length are in good agreement with the experimental evidence. Regarding wheel W1, numerical simulation is overestimating the damage prediction, showing a complete failure of the rim in the hump region, which anyway confirms that the impact test is critical for this wheel type as highlighted by the result of one experimental test of Fig. 27.

By comparing Fig. 28 and Fig. 29, it can be observed that the two methods employed for the prediction of the failure of the wheel are in rather good agreement. In fact, both models correctly identify the location where the cracks appear in the experimental tests and identify W1 as more critical than W3. The strain energy density method seems to underestimate the crack length and includes also part of the flange rim which acutually does not show any crack in the experimental tests. The Johnson-Cook damage model is more accurate in the crack location. However, for W1 it overestimate the crack length. This overestimation is probably due to the chosen material parameters. In fact, this model requires a set of additional material data that could be not available in the design phase of the rim.
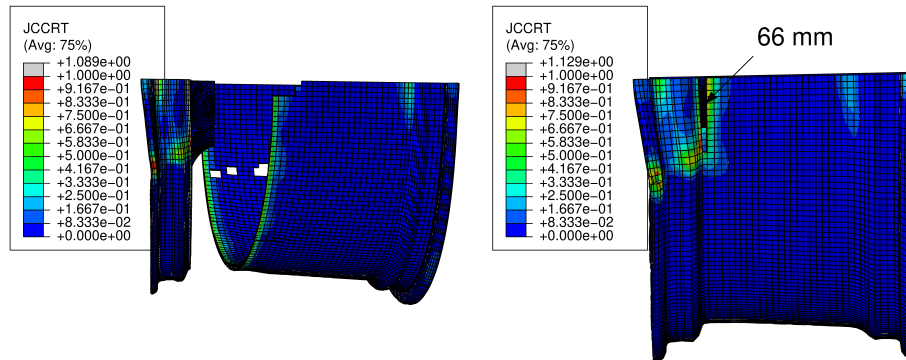
Figure 29: Contour plot of the Johnson-Cook damage parameter indicator computed on the models of wheel W1 (left) and W3(right). Element deletion is performed to model crack opening.

5. Conclusions

Our study provides wheel manufacturers with a reliable tool to simulate actual indoor impact tests. Additionally, our study suggests how an accurate tire and rim model could be implemented to simulate full vehicle crash tests when available computer power will be increased.

In the paper the simulation of the AK-LH 08 radial impact test of automotive wheels is presented and validated. The study focuses on cast aluminium alloy wheels.

The model is built by considering tyre, wheel, striker and supporting structure. Particular attention has been devoted to the definition of the tyre model. In fact, in the radial impact test the tyre plays a crucial role in the transmission of the impact forces between striker and wheel. Moreover, the tyre is subjected to very large radial deformation having its sides completely folded when the higher value of the impact force is reached. To correctly model the tyre, the cross section has been measured by means of a 3D measuring arm and modelled in the finite element software. The different portions of the tyre carcass, i.e. the sidewall, the tread and the undertread, have been modelled with a hyperelastic Mooney-Rivlin material. The 90-degree ply and the $\pm$ 20-degree steel belts have

been modelled through layers of fiber reinforcements embedded in the tyre carcass. The tyre damping has been modelled through a Rayleigh model. Simple static and dynamic tests able to provide the necessary data to calibrate material and damping parameters of the tyre have been described. The tyre model represents a balance between model complexity and accurate computation of the transmitted forces.

The wheel has been modelled by means of an elasto-plastic isotropic material. Different stress/strain curves have been assigned to the wheel rim and the spokes in order to account for the material inhomogeneity related to the wheel manufacturing process. The striker and the supporting structure have been modelled as rigid bodies.

A two phases experimental campaign has been realized for the validation of the modelling procedure. In the first phase a wheel rim has been instrumented by strain gauges and subjected to high and low energy impact tests. The comparison between experimental and numerical results showed that for the low energy test a good agreement has been obtained. For the high energy test, the accuracy of the numerical model is slightly lower, especially for what concerns the acceleration on the striker and the impact force. Referring to the strains, the maximum difference is around 14% on the wheel rim which is the most critical zone of the wheel. A very good prediction of the residual deformation of the inboard rim flange of the wheel rim has been obtained with a 8% difference between experimental and numerical results. This deformation is very important as represents the actual output of the test and the pass criteria.

In the second phase of the experimental validation, four additional wheel types have been tested, in some cases repeating the tests on different wheel specimens. A total of nine wheels have been tested at high and low energy levels. The maximum impact force and the residual displacement at the internal rim flange have been compared with the numerical simulations. Comparison has shown a difference of less than $\pm 10\%$ for the majority of the tested wheels.

Two out of the five tested wheel types exhibited fractures on the wheel rim. In most of the cases, cracks were located near the outboard hump and

in one case at the outboard rim flange. The damage mechanism of the wheels has been modelled in two different ways. At a first attempt, the total plastic strain energy density has been considered as a damage indicator in the numerical model. These failures have been quite well predicted by the developed numerical model, both referring to location and dimensions. Secondly, element deletion has been implemented in numerical models to simulate the physical process of cracks opening. A Johnson-Cook damage model has been employed to model damage initiation, with material parameters taken from the literature. Results showed that this second approach is more effective in capturing both crack locations and size than the strain energy density method. The two methods employed for the prediction of the failure of the wheel show a rather good agreement.

Acknowledgements

References

[1] F. Ballo, R. Frizzi, G. Mastinu, D. Mastroberti, G. Previati, C. Sorlini, Lightweight Design and Construction of Aluminum Wheels, in: SAE Technical Paper, SAE International, doi:\bibinfo{doi}{10.4271/2016-01-1575}, 2016.

[2] F. Ballo, M. Gobbi, G. Mastinu, G. Previati, Motorcycle tire modeling for the study of tire-rim interaction, Journal of Mechanical Design 138 (2016) 051404–051404–13, doi:\bibinfo{doi}{10.1115/1.4032470}.

[3] U. Kocabicak, M. Firat, Numerical analysis of wheel cornering fatigue tests, Engineering Failure Analysis 8 (4) (2001) 339 – 354, ISSN 1350-6307, doi:\bibinfo{doi}{https://doi.org/10.1016/S1350-6307(00)00031-5}, URL `http://www.sciencedirect.com/science/article/pii/S1350630700000315`.

[4] F. Ballo, M. Gobbi, G. Mastinu, G. Previati, R. Zerboni, Motorcycle tire modeling, in: Proc. of the ASME 2015 IDETC/CIE 2015, Boston, Massachussetts, USA, 2015.

[5] M. Firat, R. Kozan, M. Ozsoy, O. H. Mete, Numerical modeling and simulation of wheel radial fatigue tests, Engineering Failure Analysis 16 (5) (2009) 1533 – 1541, ISSN 1350-6307, doi:\bibinfo{doi}{https://doi.org/10.1016/j.engfailanal.2008.10.005}, URL http://www.sciencedirect.com/science/article/pii/S1350630708002343.

[6] X. Wan, Y. Shan, X. Liu, H. Wang, J. Wang, Simulation of biaxial wheel test and fatigue life estimation considering the influence of tire and wheel camber, Advances in Engineering Software 92 (2016) 57 – 64, ISSN 0965-9978, doi:\bibinfo{doi}{https://doi.org/10.1016/j.advengsoft.2015.11.005}, URL http://www.sciencedirect.com/science/article/pii/S0965997815001714.

[7] F. M. Santiciolli, R. Möller, I. Krause, F. G. Dedini, Simulation of the scenario of the biaxial wheel fatigue test, Advances in Engineering Software 114 (2017) 337–347, ISSN 0965-9978, doi:\bibinfo{doi}{10.1016/J.ADVENGSOFT.2017.08.006}, URL https://www.sciencedirect.com/science/article/pii/S0965997817304350.

[8] Wheels – Lateral Impact Test Procedures – Road Vehicles, SAE J175, sAE standards, 2016.

[9] Road Vehicles – Light alloy wheels – Impact test, ISO 7141, iSO standards, 2005.

[10] Räder – Anforderungen und Prüfungen, Arbeitskreis Lastenheft, Arbeitskreis-Lastenheft AK-LH 08, arbeitskreis der Firmen: Audi AG, Bayerische Motorenwerke AG, DaimlerChrysler AG, Porsche AG, Volkswagen AG, 2006.

[11] R. Neves, G. Micheli, M. Alves, An experimental and numerical investigation on tyre impact, International Journal of Impact Engineering 37 (6) (2010) 685 – 693, ISSN 0734-743X, doi:\bibinfo{doi}{https://doi.org/10.1016/j.ijimpeng.2009.10.001}, URL http://www.sciencedirect.com/science/article/pii/S0734743X09001821, impact Loading of Lightweight Structures.

[12] C.-L. Chang, S.-H. Yang, Simulation of wheel impact test using finite element method, Engineering Failure Analysis 16 (5) (2009) 1711 – 1719, ISSN 1350-6307, doi:\bibinfo{doi}{https://doi.org/10.1016/j.engfailanal.2008.12.010}, URL http://www.sciencedirect.com/science/article/pii/S1350630709000028.

[13] M. Cerit, Numerical simulation of dynamic side impact test for an aluminium alloy wheel, Scientific Research and Essays 5 (18) (2010) 2694 – 2701.

[14] R. Shang, W. Altenhof, N. Li, H. Hu, Wheel impact performance with consideration of material inhomogeneity and a simplified approach for modeling, International Journal of Crashworthiness 10 (2) (2005) 137–150, doi:\bibinfo{doi}{10.1533/ijcr.2005.0333}.

[15] S. Ishikawa, Y. Sakai, N. Nosaka, Application of Impact Analysis for Aluminum Wheel with Inflated Tire, in: Proceedings of 2014 SIMULIA Community Conference, 2014.

[16] M. B. K, V. S, S. Srinivasan, A. Nesarikar, Simulation and Test Correlation of Wheel Impact Test, in: SAE Technical Paper, The Automotive Research Association of India, doi:\bibinfo{doi}{10.4271/2011-28-0129}, URL https://doi.org/10.4271/2011-28-0129, 2011.

[17] X. M. Yuan, L. J. Zhang, X. Y. Chen, B. Du, B. H. Li, L. G. Fan, Y. Pan, Numerical Simulation of Aluminum Alloy Wheel 13 ° Impact Test Based on Abaqus, in: Advances in Design Technology, vol. 215 of *Applied Mechanics*

and Materials, Trans Tech Publications, 1191–1196, doi:\bibinfo{doi}{10. 4028/www.scientific.net/AMM.215-216.1191}, 2012.

[18] E. Tönük, Y. Ünlüsoy, Prediction of automobile tire cornering force characteristics by finite element modeling and analysis, Computers and Structures 79 (2001) 1219–1232.

[19] G. Holzapfel, Nonlinear Solid Mechanics: A continuum Approach for Engineering, Wiley, 2000.

[20] K. Tan, S. Wong, R. Radin Umar, A. Hamouda, N. Gupta, An experimental study of deformation behaviour of motorcycle front wheel-tyre assembly under frontal impact loading, International Journal of Impact Engineering 32 (10) (2006) 1554–1572, ISSN 0734-743X, doi: \bibinfo{doi}{10.1016/J.IJIMPENG.2005.04.007}, URL `https://www.sciencedirect.com/science/article/pii/S0734743X05000734`.

[21] K. S. Tan, S. V. Wong, R. S. Radin Umar, A. M. S. Hamouda, N. K. Gupta, Impact behavior modeling of motorcycle front wheel-tire assembly, International Journal of Automotive Technology 10 (3) (2009) 329–339, ISSN 1976-3832, doi:\bibinfo{doi}{10.1007/s12239-009-0038-9}, URL `https://doi.org/10.1007/s12239-009-0038-9`.

[22] F. Ballo, R. Frizzi, M. Gobbi, G. Mastinu, G. Previati, C. Sorlini, Numerical and Experimental Study of Radial Impact Test of an Aluminum Wheel: Towards Industry 4.0 Virtual Process Assessment, in: International Design Engineering Technical Conferences and Computers and Information in Engineering Conference, Volume 3: 19th International Conference on Advanced Vehicle Technologies; 14th International Conference on Design Education; 10th Frontiers in, ASME, 1–10, doi:\bibinfo{doi}{10.1115/DETC2017-67703}, 2017.

[23] Simulia, Abaqus 6.12 Analysis User's Manual, 28.1.5, 2012.

[24] D. Barbani, M. Pierini, N. Baldanzini, FE modelling of a motorcycle tyre for full-scale crash simulations, International Journal of Crashworthiness 17 (3) (2012) 309–318, ISSN 13588265, doi:\bibinfo{doi}{10.1080/13588265.2012. 661212}.

[25] F. Ballo, G. Previati, M. Gobbi, G. Mastinu, Tire-rim interaction, a semi-analytical tire model, Journal of Mechanical Design 00000 (2018) 1–12, ISSN 1050-0472, doi:\bibinfo{doi}{10.1115/ 1.4038927}, URL http://mechanicaldesign.asmedigitalcollection. asme.org/article.aspx?doi=10.1115/1.4038927.

[26] F. Ballo, M. Gobbi, G. Mastinu, G. Previati, Advances in Force and Moments Measurements by an Innovative Six-axis Load Cell, Experimental Mechanics 54 (4) (2014) 571–592, ISSN 17412765, doi:\bibinfo{doi}{10. 1007/s11340-013-9824-4}.

[27] S. Rao, Mechanical Vibrations, Prentice Hall, 2011.

[28] B. S. Kim, C. H. Chi, T. K. Lee, A study on radial directional natural frequency and damping ratio in a vehicle tire, Applied Acoustics 68 (5) (2007) 538 – 556, ISSN 0003-682X, doi:\bibinfo{doi}{https://doi.org/10.1016/j. apacoust.2006.07.009}, URL http://www.sciencedirect.com/science/ article/pii/S0003682X06001654.

[29] Z. Geng, A. Popov, D. Cole, Measurement, identification and modelling of damping in pneumatic tyres, International Journal of Mechanical Sciences 49 (10) (2007) 1077 – 1094, ISSN 0020-7403, doi:\bibinfo{doi}{https://doi. org/10.1016/j.ijmecsci.2007.03.004}, URL http://www.sciencedirect. com/science/article/pii/S0020740307000495.

[30] A. A. Popov, Z. Geng, Modelling of vibration damping in pneumatic tyres, Vehicle System Dynamics 43 (sup1) (2005) 145–155, doi:\bibinfo{doi}{10. 1080/00423110500140765}.

[31] R. Pelle, FEM Simulation of the Tire/Rim Seating Process, Tire Science and Technology 22 (1994) 76–98.

[32] J. D. Reida, D. A. Boesch, R. W. Bielenberg, Detailed tire modeling for crash applications, International Journal of Crashworthiness 12 (5) (2007) 521–529, ISSN 13588265, doi:\bibinfo{doi}{10.1080/13588260701483813}.

[33] F. Orengo, M. Ray, C. Plaxico, Modeling tire blow-out in roadside hardware simulations using LS-DYNA, in: ASME International Mechanical Engineering Congress, Washington, D.C., USA, ISBN 0791837300, 71–80, doi:\bibinfo{doi}{10.1115/IMECE2003-55057}, URL `http://proceedings.asmedigitalcollection.asme.org/proceeding.aspx?articleid=1595678`, 2003.

[34] X. Teng, T. Wierzbicki, Evaluation of six fracture models in high velocity perforation, Engineering Fracture Mechanics 73 (12) (2006) 1653–1678, ISSN 0013-7944, doi:\bibinfo{doi}{10.1016/J.ENGFRACMECH.2006.01.009}, URL `https://www.sciencedirect.com/science/article/pii/S0013794406000427`.

[35] Y. Bao, T. Wierzbicki, A Comparative Study on Various Ductile Crack Formation Criteria, Journal of Engineering Materials and Technology 126 (3) (2004) 314, ISSN 00944289, doi:\bibinfo{doi}{10.1115/1.1755244}, URL `http://materialstechnology.asmedigitalcollection.asme.org/article.aspx?articleid=1427232`.

[36] G. R. Johnson, W. H. Cook, Fracture characteristics of three metals subjected to various strains, strain rates, temperatures and pressures, Engineering Fracture Mechanics 21 (1) (1985) 31–48, ISSN 0013-7944, doi:\bibinfo{doi}{10.1016/0013-7944(85)90052-9}, URL `https://www.sciencedirect.com/science/article/pii/0013794485900529`.

[37] H. Mae, X. Teng, Y. Bai, T. Wierzbicki, Calibration of ductile fracture properties of a cast aluminum alloy, Mater. Sci. Engng A 459 (1-2) (2007) 156–166.

[38] H. Mae, X. Teng, Y. Bai, T. Wierzbicki, Comparison of ductile fracture properties of aluminum castings: Sand mold vs. metal mold, International Journal of Solids and Structures 45 (5) (2008) 1430–1444, ISSN 00207683, doi:\bibinfo{doi}{10.1016/j.ijsolstr.2007.10.016}.